One-axis Two-wing Guest-Host Strategy for Constructing Ultralong-lifetime Near-infrared Organic Phosphorescence Materials for Bioimaging

Fuming Xiao
Wenzhou University
Heqi Gao
Nankai University
Yunxiang Lei
Wenzhou University
Wenbo Dai
Beijing Institute of Technology
Miao-Chang Liu
Wenzhou University
Xiaoyan Zheng
Beijing Institute of Technology https://orcid.org/0000-0002-6584-9596
Zhengxu Cai
Beijing Institute of Technology https://orcid.org/0000-0003-0239-9601
Xiaobo Huang
Wenzhou University
Hua-yue wu
Wenzhou University
Dan Ding (dingd@nankai.edu.cn)
Nankai University https://orcid.org/0000-0003-1873-6510

Article

Keywords: room temperature phosphorescence (RTP), optics

Posted Date: July 12th, 2021

DOI: https://doi.org/10.21203/rs.3.rs-650507/v1

Version of Record: A version of this preprint was published at Nature Communications on January 10th, 2022. See the published version at https://doi.org/10.1038/s41467-021-27914-0.

Abstract

Organic near-infrared room temperature phosphorescence (RTP) materials have unparalleled advantages in bioimaging due to their excellent penetrability. However, limited by the energy gap law, organic matters with long wavelengths (> 700 nm) and long lifetimes (> 100 ms) have not been reported so far. In this work, we have obtained organic RTP materials with long wavelengths (657–732 nm) and long lifetimes (102–324 ms) for the first time through the one-axis two-wing guest-host strategy. The one axis refers to that the guest molecule has sufficient conjugation to reduce the lowest triplet energy level and the two wings refer to that the host assists the guest in exciton transfer and inhibits the non-radiative transition of guest excitons. These materials exhibit good tissue penetration in bioimaging. Thanks to the characteristic of long lifetime and long wavelength emissive RTP materials, the tumor imaging in living mice with a signal to background ratio value as high as 43 is successfully realized. This work provides a practical solution for the construction of organic RTP materials with both long wavelengths and long lifetimes.

Introduction

Room-temperature phosphorescence (RTP) of organic materials with persistent emissions can mitigate the interference from environmental self-luminescence. Moreover, organic matter often has advantages of low toxicity and good biocompatibility.[1–10] Therefore, constructing organic RTP materials would benefit tissue imaging, tumor diagnosis, and drug tracking.[10–15] To date, most phosphorescent materials have poor biological tissue permeability because the wavelengths of their emission spectra are short (less than 580 nm).[16–27] This only means phosphors provide good imaging in shallow regions of an organism. Constructing near-infrared phosphorescent materials has gained some urgency. Although some red RTP materials such as boron fluoride, carbazole, and naphthalene diimides have been developed, those with wavelengths exceeding 650 nm are rare.[28–33] Moreover, presumably limited by the energy gap law, phosphorescence lifetimes of these red RTP materials are very short and not conducive for bioimaging (Scheme 1a, Supplementary Scheme S1).

Establishing ultralong-lifetime RTP materials with long-wavelength emission inevitably means lowering the lowest triplet (T_1) level of the material. However, lower T_1 levels bring two major obstacles to phosphorescence. One of the obstacles is that lower T_1 increases the band gap between S_1 and T_1 (ΔE_{ST}), which is not conducive to intersystem crossing (ISC) of excitons. The other obstacle is that a lower T_1 level easily causes excitons to be consumed non-radiatively, resulting in a significant reduction in lifetime and intensity of phosphorescence (Scheme 1b). Therefore, assuming materials already have low T_1, improving the ISC capability of excitons and suppressing the non-radiative transitions of excitons are key in achieving ultralong-lifetime near-infrared phosphorescence. Recently, guest–host materials have gradually attracted more attention,[34–41] because the host molecules can inhibit the non-radiative transition of the guest energy in the guest–host system.[42–47] Additionally, several research results have shown that there is a synergy of energy between host and guest molecules, which can assist the guest

molecules to transfer the excited state energy effectively.[39–43] Therefore, the guest–host system provides a new strategy for the construction of organic RTP materials with long-wavelength emissions and long lifetimes.

With that in mind, we tried to construct ultralong-lifetime near-infrared RTP materials employing a one-axis two-wing guest–host strategy. The guest pyrene derivatives with high conjugation are regarded as the central axis. Their high conjugation can reduce the T_1 levels of the molecules, thereby ensuring that the resultant materials undergo long-wavelength phosphorescence. The benzophenone (**BPO**) compound is chosen as the host matrix, which can act as two wings. One wing is associated with assisting transfers of guest excitons; the other wing is associated with restricting the motion of the guest molecules, thereby suppressing the non-radiative transition of guest excitons (Scheme 1c). The results show that the designed guest–host materials have strong red afterglow visible to the naked eye. By increasing the degree of conjugation of the guest molecules, phosphorescence wavelengths of the guest–host materials are red-shifted from 657 nm to 732 nm. More importantly, our newly developed guest–host materials have long phosphorescence lifetimes of 102–324 ms. To the best of our knowledge, this is the first RTP material with both long wavelength (> 700 nm) and long lifetime (> 100 ms). Comparative experiments of the molten state and the crystalline state prove that the host matrix restricts the motion of guest molecules is a necessary condition for the doped system to have phosphorescence emission. Molecular dynamics (MD) simulations further show that between host and guest there is a strong interaction that suppresses non-radiative transitions of guest excitons. Moreover, experimental results also confirm that host molecules exhibit synergies with guest molecules in excited states. As a proof-of-concept, the materials were used for precise mapping of lymph nodes and labeling of armpit tumors with high signal-to-background ratios (SBR) of 55 and 43, respectively. The long wavelengths help to reduce scattering from tissue and long lifetimes further mitigate the interference from autofluorescence in bioimaging. Thus, phosphorescent materials with both kinds of properties can provide more unambiguous imaging of tumors.

Results And Discussion

The guest molecules are based on the pyrene unit, to which adding anisole or *N,N*-dimethylaniline groups on one or both sides through the Suzuki reaction increases the molecular conjugation (Fig. 1a, Supplementary Scheme S2). The five guests show good solubility in chloroform, tetrahydrofuran, and dimethyl sulfoxide. The molecular structures and purities of the target compounds were confirmed by NMR spectroscopy, single-crystal X-ray diffraction, and high-performance liquid chromatography (Supplementary Fig. S1, Fig. S2). As guest conjugation increases, the maximum absorption peaks are red-shifted from 343 nm to 378 nm (Supplementary Fig. S3a), and the corresponding fluorescence peaks are also red-shifted from 381 nm to 467 nm (Supplementary Fig. S3b). The host BPO was purchased directly from a commercial supplier and used without further processing. BPO has a low melting point (48 ℃) and stable subcooling states and thus the guest molecules can be dispersed in the host using the melt-casting method. Because the concentration of the guest molecules is very important in determining the

RTP properties of the guest–host materials, we first prepared a series of **Py/BPO** guest–host materials with different guest–host molar ratios (1:50–1:50000) to optimize the luminescence performance. The strongest phosphorescence intensity was obtained with the guest–host molar ratio of 1:1000 (Supplementary Fig. S5), which is in accordance with our previous work.[40–43] Four other guest–host materials (**MOPy/BPO**, **MAPy/BPO**, **DMOPy /BPO**, and **DMAPy/BPO**, Fig. 1a) with a guest–host molar ratio of 1:1000 were prepared, and the luminescence characteristics of the guest–host systems were systematically investigated.

Five guest–host materials show blue to cyan fluorescence under the excitation source (Fig. 1b) and the maximum emission peaks of the guest–host materials are red-shifted from 416 nm to 483 nm as guest conjugation increases (Table 1, Supplementary Fig. S6). Importantly, after finishing the irradiation, with the exception of **DMAPy/BPO**, the other four guest–host materials have visible to the naked eye a deep red afterglow for approximately 3 s that reveal the RTP properties (Fig. 1b). Delayed spectra further show that the guest–host materials have two phosphorescence peaks, which are fine structures that arise from energy level vibrations. Similarly, with increasing guest conjugation, the phosphorescence peaks of the guest–host materials are red-shifted from 657 nm to 732 or 600 nm to 681 nm (Table 1, Fig. 1c). That is, the guest–host materials produce deep-red or even near-infrared phosphorescence emissions and belong to a group that produce phosphorescence with the longest wavelengths to date. The Commission Internationale de l'Eclairage coordinates further indicate that the guest–host materials have a very deep phosphorescent color (0.63, 0.35; 0.64, 0.34; 0.65, 0.33; 0.69, 0.30; 0.70, 0.29) (Supplementary Fig. S7). Unlike most red RTP materials which have short phosphorescence lifetimes, the phosphorescence lifetimes of this guest–host system are 102–324 ms (Table 1, Fig. 1d). Moreover, the guest–host materials have satisfactory luminous intensities, the phosphorescence quantum efficiency being in the range 4.2%–9.2% (Table 1). The above results fully prove that, with the one-axis two-wing guest–host strategy, we have developed a group of ultralong-lifetime near-infrared RTP materials.

Table 1. Photophysical data of the guest–host materials

Sample	Fluo.			Phos.		
	λ_{em} (nm)	Φ_F (%)	τ (ns)	λ_{em} (nm)	Φ_P (%)	τ (ms)
Py/BPO	415	14.2	1.43	600, 657	9.2	327, 324
MOPy/BPO	424	13.4	2.03	623, 680	8.0	215, 210
MAPy/BPO	440	15.2	1.98	643, 697	6.3	201, 198
DMOPy/BPO	471	12.3	2.19	657, 713	5.4	180, 175
DMAPy/BPO	483	16.1	2.32	681, 732	4.2	106, 102

Generally, the triplet excitons are unstable and easily assimilated by the motion of molecules, leading to the quenching of phosphorescence. However, for the guest–host system, the host matrix can provide a rigid environment to restrict the motion of guest molecules, thereby ensuring the guests emit phosphorescence.[43,44] We first register the phosphorescence of the guest molecules at low temperature (77 K) to verify that the phosphorescence from the guest–host system is emitted by the guest molecules. The spectra show that the guests have two fine peaks at 77 K, and the emission peaks are also red-shifted from 596 nm to 665 nm or 652 nm to 725 nm (Supplementary Fig. S10). The spectral data are almost completely consistent with the phosphorescence wavelengths of the corresponding doped materials. The results confirm that the phosphorescence in the guest–host system is emitted by the guest molecules. Taking advantage of the low melting point of the host, the influence of the host morphology on the phosphorescence performance of the guest–host system was analyzed. The **Py/BPO** molten state at room temperature (subcooling state) show only fluorescence but no phosphorescence (Fig. 2a, Fig. 2b). However, when the guest–host material begins to crystallize, the material produces a bright red phosphorescence. This clearly proves that the host matrix restricts the guest molecular motion and is a necessary factor in determining the RTP properties of the guest–host system.

The local microenvironment of the molecules such as the molecular configuration, intermolecular distance, and intermolecular interaction plays an important role in determining the photophysical phenomena of materials. However, obtaining the co-crystal of host-guest is difficult because of the trace amounts of guest molecules (≤0.1 %) in the entire materials. Moreover, the traditional characterization methods such as X-ray diffractometry, scanning electron microscopy, and transmission electron microscopy are difficult to apply in investigating the molecular conformation of the guests in the host matrix in detail. Therefore, we simulated the molecular conformations of **Py** molecules in the **BPO** matrix using MD simulations.[41] The initial **Py/BPO** model was based on the **BPO** crystal. A **BPO** molecule is removed from the **BPO** crystal (Fig. 2c) and a **Py** molecule inserted into the vacancy. This **Py/BPO** model has a 1:191 molar ratio of **Py** to **BPO**. Starting from the initial Py/BPO configuration, we performed production MD simulations for 10-ns to relax the whole guest–host system using GROMACS software package (version 5.1.5, details in SI). Compared with the conformations of **BPO** molecules in a single crystal, the corresponding conformations of the **BPO** molecules adjacent to the guest **Py** molecule in the **Py/BPO** guest–host system are slightly different because twisting increases the angles slightly after doping (Supplementary Fig. S11). This is because the spatial volume of the **Py** molecule is larger than that of the **BPO** molecule. However, because the number of guest/**Py** in the guest–host system is very small, the impact on the overall arrangement of the host matrix is minimal. Therefore, the stacking of **BPO** molecules in the simulated guest–host system is almost the same as for a single crystal (Supplementary Fig. S12, S13). The XRD results also confirm little change in the arrangement of the **BPO** host before and after doping with guest molecules (Supplementary Fig. S14). Therefore, we have a microenvironment model of the guest–host system that is reasonable and reliable for our MD simulations.

With this **Py/BPO** model, we first analyzed the relative spatial positions of the Py molecule in the **BPO** matrix (Fig. 2d). The distances between the guest and host molecules in the six directions (up, down, front, back, left, and right) range from 2.3 Å to 3.1 Å. That is, the guest molecules are in a relatively dense matrix environment, which can effectively inhibit their motion. More importantly, although these distances are relatively similar, the host has a twisted molecular conformation. Therefore, there is no π–-π interaction between host and guest, and hence it is not conducive for luminescence. In contrast, between the host and **Py** molecules, multiple C-H–-π interactions are evident over short distances (2.3 Å–3.2 Å, red line) (Fig. 2e), and the average distance between a **Py** molecule and surrounding host molecules is only 2.77 Å. In addition, the C-H–-O interactions between Py and host molecules are also evident over short distances (2.5 Å and 2.6 Å, blue line) (Fig. 2e). The above analysis shows that the the **Py**-doped host matrix provides a relatively close and strong interactive environment for guest molecules that effectively restricts the non-radiative decay channels.

The rigid environment provided by the matrix is necessary for the guest–host system to display RTP characteristics. However, is this the only role the host molecules play? We chose separately as host sulfonyldibenzene (**SOB**), sulfinyldibenzene (**SIB**), and diphenylphosphine oxide (**PPO**), which also have good crystallinity and a similar structure to **BPO** (Fig. 3a), and **MAPy** as guest. The three guest–host materials (**MAPy/SOB**, **MAPy/SIB**, and **MAPy/PPO**) were prepared with a guest–host molar ratio of 1:1000. Unfortunately, although these materials have strong cyan fluorescence under a UV lamp, no red afterglow appears once the UV source is removed (Fig. 3b). The fluorescence spectra of the three guest–host materials show wavelengths centered around 430 nm (Supplementary Fig. S15a), with quantum yields as high as 63%, 71% and 76% in the order given above. Such high luminous intensities indicate that the host indeed inhibits the motion of the guest molecules. However, the delayed spectra suggest that the guest–host materials have almost no phosphorescence emission (Supplementary Fig. S15b). Note that, although the phosphorescence from **MAPy/SOB** and **MAPy/SIB** are very weak, there is an emission peak near 670 nm that once again demonstrates that the phosphorescence in the guest–host material is emitted by the guest molecules. The above comparative experiments show that the rigid restrictive environment provided by the host is a necessary but not a sufficient factor, for the guest host materials to display RTP properties.

Energy transfers between host and guest molecules have gradually been revealed to play a vital role in phosphorescence activity. Among them, Förster resonance energy transfer (FRET) is considered a viable explanation why some guest–host materials have RTP properties.[24,39] To verify whether there is a FRET between host and guest, the absorption and excitation spectra of host **BPO** and guest MAPy were investigated. The absorption and excitation wavelengths of host **BPO** (Fig. 4a) only reach 418 nm, whereas the absorption and excitation wavelengths of the guest **MAPy** reach 465 nm. Therefore, we investigated the phosphorescence emission of **MAPy/BPO** material at different excitation wavelengths. The results show that even if the excitation wavelength is extended to 440 nm, the **MAPy/BPO** powder maintains a strong phosphorescence emission (Fig. 4b) and has a red afterglow visible to the naked eye after removing the 420-nm UV source (Fig. 4c). These results clearly demonstrate that the

phosphorescence of **MAPy/BPO** does not come from the energy absorbed by the host matrix, but from the energy absorbed by the guest molecules. Therefore, a FRET between host and guest is ruled out.

In our previous work, we found that the host could assist the excitons of the guests in energy transfer.[41–43] We therefore recorded the excitation spectra (fluorescence emission/420 nm) of guest **MAPy** in common solvents (toluene, THF, and *N,N*-dimethylformamide/DMF) and host **BPO** (molten state and crystal state). The results (Fig. 4d) show that the maximum excitation wavelength in **MAPy** emissions in these solvents is 346 nm, whereas the maximum excitation wavelengths in host emissions in the molten and crystalline states are red-shifted to 392 nm and 387 nm, respectively. The excitation spectra of the phosphorescence emission (660 nm) also show that the maximum excitation wavelengths in emissions from **MAPy** in these solvents are significantly longer than that of the crystalline host (Fig. 4e). Hence, we conclude that the host not only acts as the rigid matrix, but also changes the energy transfer process for the guest in the excited state. Furthermore, the phosphorescence lifetimes of guest molecules at 77 K are only between 12 ms – 23 ms (Fig. 4f), which are much shorter than that of the host matrix. This also shows that the host matrix prolongs the ISC process of the guest excitons.

From the above experimental results and our previous work,[41–43], we conjecture that the T_1 of the host is the bridge between S_1 and T_1 of the guest (Fig. 4g), and hence the excited energy from the guest is transferred from S_1 to T_1 of the guest via the T_1 path of the host. To verify this mechanism, density functional theory calculations were performed to obtain the singlet and triplet energy levels of the host and guest molecules. The energy range for the S_1 and T_1 states of the five guest molecules are 3.01–3.49 eV and 1.84–2.15 eV, respectively (Fig. 4h). The ΔE_{ST} of the guest molecules are in the range of 1.17–1.34 eV; such large energy gaps make excitonic ISC difficult. However, the band gaps between the S_1 state of the guests and the T_1 state of the host are only 0.11–0.59 eV (Fig. 4h), which is advantageous for excitonic ISC. Therefore, the synergy action for the guest–host system is also an important factor in the phosphorescence activity of guest–host materials.

Long-wavelength emissions are well-known to be beneficial in reducing tissue scattering and enhancing tissue penetration, and thus improve bio-imaging quality. Encouraged by the excellent properties of these near-infrared RTP materials, an application to bioimaging was investigated. Because **DMAPy/BPO** among the materials studied exhibits the longest wavelength with a quite long lifetime, **DMAPy/BPO** and the biocompatible amphiphilic copolymer PEG-b-PPG-b-PEG (F127) were selected as nanoparticle (NP) cores and the encapsulation matrix, respectively. To ensure our **DMAPy/BPO** NPs were accessible in vivo with good RTP performance, a top-down method was employed to produce the NPs.[48,49] To verify the advantages of long-wavelength RTP materials, a short-wavelength ($\lambda_{Phos.}$ = 520 nm) but strong intensity ($\Phi_{Phos.}$ = 64 %) RTP material **DOB/BPO** reported in our previous work was selected as a control and **DOB/BPO** NPs were prepared by the same method.[50] Dynamic light scattering and transmission electron microscopy data indicated both **DMAPy/BPO** and **DOB/BPO** NPs formed a near-spherical morphology with a mean hydrodynamic diameter of ≈ 100 nm (Fig. 5a and Supplementary Fig. S16). Both kinds of NPs revealed strong resistance to photobleaching, indicative of little change in their intensities after eight

cycles of stimulation or eighty minutes of 365-nm UV light irradiation. (Fig. 5b, Supplementary Figs. S17 and S18) We further verified the quantitative conversion of the phosphorescence intensity with NP concentrations. The phosphorescence intensities of **DMAPy/BPO** NPs and **DOB/BPO** NPs were captured at t = 10 s post-excitation, and possess good linearity with the NP concentration (Fig. 5c, Supplementary Fig. S19). **DMAPy/BPO** NPs and **DOB/BPO** NPs display the main phosphorescence signals (Fig. 5d) under Dsred (575–650 nm) and GFP (515–575 nm) filters, respectively. This result is consistent with their phosphorescence spectra.

As tissue penetration is a considerable challenge for in vivo bioimaging, tissue penetration depths of the NPs were compared between **DMAPy/BPO** NPs and **DOB/BPO** NPs. The phosphorescence signals of both **DMAPy/BPO** NPs and **DOB/BPO** NPs (Fig. 5e and 5f) decreased with increasing thickness of chicken breast tissue. With the advantages of RTP materials, ultra-high SBR signals were observed without covering the breast tissue. However, the inherent limit with short wavelengths leads to a relatively low tissue penetration (SBR=5.4 at thickness 7.5 mm). In contrast, the NIR phosphorescence signal of the **DMAPy/BPO** NPs can still be detected (SBR=15) under a 12.5-mm thick coverage of breast tissue. This result revealed excellent deep tissue imaging from NIR emissions of NPs and moreover without excitation.

After we verified that both kinds of NPs had good cytocompatibility (Fig. 5g), we investigated phosphorescent performance of **DMAPy/BPO** NPs in various metal ions (widespread in vivo) and tissue homogenates to confirm bioimaging feasibility in vivo. After 1 min-long irradiation using a 365-nm handheld UV lamp, the phosphorescence signals of **DMAPy/BPO** NPs incubated with different metal ions were recorded immediately under the same conditions using an IVIS bioimaging instrument. However, ferric ions (including Fe^{2+} and Fe^{3+}) were found to quench the phosphorescence signals significantly compared with the signals in Na^{+} (Fig. 5h). This result might be attributed to the interaction between ferric ions with outer vacant orbitals and O/N heteroatoms with lone pair electrons in **DMAPy/BPO** NPs.[51] Furthermore, the **DMAPy/BPO** NPs were found to exhibit different phosphorescence quench behaviors in different tissue homogenates and blood (Fig. 5i). Compared with the phosphorescence signal in PBS, the signals of **DMAPy/BPO** NPs were significantly quenched in blood and blood-rich-tissues (such as heart and liver) through the quenching of Fe^{2+} and Fe^{3+} ions, which would be beneficial when imaging tumors.

Applications in intravital phosphorescence imaging were investigated. The solutions of **DMAPy/BPO** NPs and **DOB/BPO** NPs were subcutaneously injected into Balb/c nude mice, followed by imaging with an IVIS instrument in bioluminescent mode after 1-min irradiation from the 365 nm handheld UV lamp. The images were captured 10 s after the removal of the light source. To ensure the biosafety of the UV irradiation procedure, the phosphorescence signals were activated by the handheld UV lamp at 10 mW cm^{-2} power density, which is below the maximum power exposure allowed for skin irradiation (18 mW cm^{-2}).[48] For comparison, fluorescence signals derived from **DMAPy/BPO** NPs and **DOB/BPO** NPs were also evaluated, simultaneously. The subcutaneous phosphorescence imaging result (Fig. 6a) in living

mice reveals that both phosphorescent signals from **DMAPy/BPO** and **DOB/BPO** NPs can be observed at 10 s after excitation. The SBR of **DMAPy/BPO** NPs and **DOB/BPO** NPs subcutaneous phosphorescence imaging at 10 s are 160 and 75 (Fig. 6b), respectively. In contrast, the fluorescence signals of **DMAPy/BPO** NPs and **DOB/BPO** NPs were hardly distinguished from the tissue autofluorescence. We note that, although the skin thickness of mice is just approximately 0.5 mm, short-wavelength-emitting **DOB/BPO** NPs exhibit a lower SBR than **DMAPy/BPO** NPs in subcutaneous phosphorescence imaging because of scattering from skin tissue. These results are in accordance with Fig. 5e and f and also demonstrate that long-wavelength emissions from **DMAPy/BPO** can effectively decrease tissue scattering and provide high-quality phosphorescence bioimaging. The phosphorescence imaging of lymph nodes was further investigated because lymph-node labeling is clinically important in guiding tumor surgery. The phosphorescence signal (Fig. 5c and 5d) of the axillary lymph node is clearly evident (SBR = 55) whereas the fluorescence signal is not distinguishable. Thus, the lymph-node imaging confirms the effectiveness of **DMAPy/BPO** NPs for phosphorescence tissue imaging.

Precise identification of complicated diseases such as cancer calls for high-performance imaging. Encouraged by the good performance of lymph-node imaging, we evaluated the phosphorescence imaging capability in cancer diagnosis in vivo. To probe the feasibility of using long-wavelength RTP materials in such circumstances, the armpit-tumor-bearing mice were prepared with 4T1 breast cancer cells. A solution of **DMAPy/BPO** NPs was injected through the tail vein into live mice. At 6 h post-injection, the signals of **DMAPy/BPO** NPs were activated by UV light for 1 min. Next, after removal of the UV lamp excitation, phosphorescence images were captured at 10 s using the IVIS instrument in the bioluminescence mode. Similarly, fluorescence imaging was recorded at the same time for comparison. The phosphorescence signal (Fig. 6e) clearly originates from the armpit tumor. Because the NIR phosphorescence emission involves no autofluorescence interference, the SBR for the phosphorescence guided armpit tumor imaging is as high as 43 (Fig. 6f).

The mice bearing armpit tumors were sacrificed, and the main tissues were excised for ex vivo phosphorescence imaging. Reticuloendothelial system organs are known to have enriched nanomaterials. Interestingly, only liver displayed a low phosphorescence signal; in other main organs, almost no phosphorescence signal was observed (Supplementary Fig. S20). This result might be attributed to the phosphorescence signal being quenched by liver because of its abundant blood supply, which is in accordance with an earlier result (Fig. 5i). Furthermore, tissues with phosphorescence signals were collected and stained with H&E (Supplementary Fig. S21), verifying the presence of an armpit tumor. The main organs were stained with H&E as well. Compared with the main organs of PBS pre-treatment live mice, the **DMAPy/BPO** NPs did not cause obvious damage to these organs (Supplementary Fig. S22). This work confirmed that by avoiding autofluorescence interference and reducing the tissue scattering, RTP materials (**DMAPy/BPO** NPs) with both long-wavelength and long-lifetime properties can serve as potent probes for image-guided diagnosis.

Conclusion

A series of near-infrared organic RTP materials with long lifetimes were developed through a one-axis two-wing guest–host strategy. The guests with high conjugation are regarded as the central axis that ensures that the materials have low T_1 levels and long phosphorescence wavelengths. The host matrix plays a dual role in inhibiting the non-radiative transition excitons and promoting ISC of guest excitons. Through this strategy, the phosphorescence wavelength of the doped system reached 732 nm and the phosphorescence lifetime reached 102 ms. This is the first organic phosphorescent material with a long-wavelength (> 700 nm) emission and long lifetime (>100 ms). This material thus provides good tissue penetration. Furthermore, the potential of long-wavelength RTP materials as a contrast agent candidate for high-quality bioimaging was confirmed. Because tissue autofluorescence is also eliminated, the materials exhibit high-performance in both lymph node mapping and armpit tumor labeling with a high SBR of 55 and 43, respectively. This work provides a novel and feasible method for solving the non-radiative transition problem of low-energy-level excitons, and a practical solution to the construction of organic RTP materials with long-wavelength emission and long lifetimes.

Methods

Sample preparation, theoretical calculation, details of photophysical measurements, NMR spectra, bio-imaging measurement. These materials are available free of charge online at http://.....

Declarations

Acknowledgements

All animal studies were performed according to the guidelines set by the Tianjin Committee of Use and Care of Laboratory Animals, and the overall project protocols were approved by the Animal Ethics Committee of Nankai University. The accreditation number of the laboratory is SYXK(Jin) 2019-0003 promulgated by the Tianjin Science and Technology Commission.

This work was supported by the financial support from the National Natural Science Foundation of China (No 22071184, 51961160730, 51873092, and 81921004) and the Zhejiang Provincial Natural Science Foundation of China (No LY20B020014), the National Key R&D Program of China (Intergovernmental Cooperation Project, No 2017YFE0132200), and the Tianjin Science Fund for Distinguished Young Scholars (No 19JCJQJC61200).

Author contributions

Y. L, X. H. and D. D. designed the research work and revised the manuscipt. F. X. synthesized the materials. F. X. and Y. L. carried out photophysical property measurements. H. G. carried out biological tissue measurements. X. Z. carried out density functional theory calculations. Y. L, X. H. and D. D. wrote the manuscript. W. D, M. L, Z. C. and H. W. edited the manuscript. All authors discussed the results and commented on the manuscript.

References

1. Zhao, W., He, Z. & Tang, B. Z. Room-temperature phosphorescence from organic aggregates. *Nat. Rev. Mater.* **5**, 869–885 (2020).

2. Peng, Q. Ma, H. & Shuai, Z. G. Theory of long-lived room-temperature phosphorescence in organic aggregates. *Acc. Chem. Res.* **54**, 940–949 (2021).

3. Kabe, R., Adachi, C. Organic long persistent luminescence. *Nature* **550**, 384–387 (2017).

4. Gu, L., Shi, H., Bian, L. et al. Colour-tunable ultra-long organic phosphorescence of a single-component molecular crystal. *Nat. Photonics* **13**, 406–411 (2019).

5. An, Z., Zheng, C., Tao, Y. et al. Stabilizing triplet excited states for ultralong organic phosphorescence. *Nat. Mater.* **14**, 685–690 (2015).

6. Wang, X., Shi, H., Ma, H. et al. Organic phosphors with bright triplet excitons for efficient X-ray-excited luminescence. *Nat. Photonics* **15**, 187–192 (2021).

7. Bolton, O., Lee, K., Kim, H-J. et al. Activating efficient phosphorescence from purely organic materials by crystal design. *Nat. Chem.* **3**, 205–210 (2011).

8. Wang, J., Gu, X., Ma, H. et al. A facile strategy for realizing room temperature phosphorescence and single molecule white light emission. *Nat. Commun.* **9**, 2963 (2018).

9. Zhang, Y., Gao, L., Zheng, X. et al. Ultraviolet irradiation-responsive dynamic ultralong organic phosphorescence in polymeric systems. *Nat. Commun.* **12**, 2297 (2021).

10. Bian, L., Shi, H. *et al.* Simultaneously enhancing efficiency and lifetime of ultralong organic phosphorescence materials by molecular self-assembly. *J. Am. Chem. Soc.* **140**, 34, 10734–10739 (2018).

11. Ali Fateminia, S. M., Mao, Z. et al. Organic nanocrystals with bright red persistent room-temperature phosphorescence for biological applications. *Angew. Chem. Int. Ed.* **129**, 12328–12332 (2017).

12. Dang, Q., Jiang, Y., Wang, J. et al. Room-temperature phosphorescence resonance energy transfer for construction of near-infrared afterglow imaging agents. *Adv. Mater.* **32**, 2006752 (2020).

13. Wang, Y., Gao, H., Yang, J. et al. High performance of simple organic phosphorescence host-guest materials and their application in time-resolved bioimaging. *Adv. Mater.* 2007811 (2021).

14. Gao, H., Gao, Z. et al. Boosting room temperature phosphorescence performance by alkyl modification for intravital orthotopic lung tumor imaging. *Small* **17**, 2005449 (2021).

15. He, Z., Gao, H. et al. Achieving persistent, efficient, and robust room-temperature phosphorescence from pure organics for versatile applications. *Adv. Mater.* **31**, 1807222 (2019).

16. Zhang, T., Ma, X., Wu, H. et al. Molecular engineering for metal-free amorphous materials with room-temperature phosphorescence. *Angew. Chem. Int. Ed.* **59**, 11206–11216 (2020).

17. Li, J., Zhou, J., Mao, Z. et al. Transientand persistent room-temperature mechanoluminescence from a white-light-emitting AIEgen with tricolor emission switching triggered by light. *Angew. Chem. Int. Ed.* **130**, 6559–6563 (2018).

18. Wang, T., Hu, Z., Nie, X. et al. Thermochromic aggregation-induced dual phosphorescence via temperature-dependent sp^3-linked donor-acceptor electronic coupling. *Nat. Commun.* **12**, 1364 (2021).

19. Yang, Z., Xu, C., Li, W., Mao, Z. et al. Boosting the quantum efficiency of ultralong organic phosphorescence up to 52% via intramolecular halogen bonding. *Angew. Chem. Int. Ed.* 59, 17451–17455 (2020).

20. Zhang, Y., Gao, L., Zheng, X. et al. Ultraviolet irradiation-responsive dynamic ultralong organic phosphorescence in polymeric systems. *Nat. Commun.* **12**, 2297 (2021).

21. Dou, X., Zhu, T., Wang, Z. et al. Color-tunable, excitation-dependent, and time-dependent afterglows from pure organic amorphous polymers. *Adv. Mater.* **32**, 2004768 (2020).

22. Ren, J., Wang, Y. et al. Force-induced turn-on persistent room-temperature phosphorescence in purely organic luminogen. *Angew. Chem. Int. Ed.* **60**, 1–7 (2021).

23. Li, D., Lu, F., Wang, J. et al. Amorphous metal-free room-temperature phosphorescent small molecules with multicolor photoluminescence via a host-guest and dual-emission strategy. *J. Am. Chem. Soc.* **140**, 1916–1923 (2018).

24. Zhou, B. & Yan, D. P. Hydrogen-bonded two-component ionic crystals showing enhanced long-lived room-temperature phosphorescence via TADF-assisted förster resonance energy transfer. *Adv. Funct. Mater.* **29**, 1807599 (2019).

25. Nidhankar, A., Goudappagouda. et al. Self-assembled helical arrays for the stabilization of the triplet state. *Angew. Chem. Int. Ed.* **59**, 13079–13085 (2020).

26. Cai, S., Ma, H., Shi, H. et al. Enabling long-lived organic room temperature phosphorescence in polymers by subunit interlocking. *Nat. Commun.* **10**, 4247 (2019).

27. Xiao, F., Wang, M., Lei, Y. et al. Achieving crystal-induced room temperature phosphorescence and reversible photochromic properties by strong intermolecular interactions. *J. Mater. Chem. C* **8**, 17410–17416 (2020).

28. Xiao, L., Wu, Y., Yu, Z. et al. Room-temperature phosphorescence in pure organic materials: halogen bonding switching effects. *Chem. Eur. J.* **24**, 1801–1805 (2018).

29. Wu, X., Huang, C-Y., Chen, D-G. et al. Exploiting racemism enhanced organic room-temperature phosphorescence to demonstrate Wallach's rule in the lighting chiral chromophores. *Nat. Commun.* **11**, 2145 (2020).

30. Wang, X., Guo, W., Xiao, H. et al. Pure organic room temperature phosphorescence from unique micelle-assisted assembly of nanocrystals in water. *Adv. Funct. Mater.* **30**, 1907282 (2020).

31. Wang, X., Xiao, H., Chen, P. et al. Pure Organic room temperature phosphorescence from excited dimers in self-assembled nanoparticles under visible and near-infrared irradiation in water. *J. Am. Chem. Soc.* **141**, 5045−5050 (2019).

32. Ono, T., Kimura, K., Ihara, M. et al. Room-temperature phosphorescence emitters exhibiting red to near-infrared emission derived from intermolecular charge-transfer triplet states of naphthalenediimide-halobenzoate triad molecules. *Chem. Eur. J.* DOI: 10.1002/chem.202100906.

33. Katsurada, Y., Hirata, S., Totani, K. et al. Photoreversible on-off recording of persistent room-temperature phosphorescence. *Adv. Optical Mater.* **3**, 1726–1737 (2015).

34. Zhang, X., Du, L., Zhao, W. et al. Ultralong UV/mechano-excited room temperature phosphorescence from purely organic cluster excitons. *Nat. Commun.* **10**, 5161 (2019).

35. Chen, C., Chi, Z., Chong, K. C. et al. Carbazole isomers induce ultralong organic phosphorescence. *Nat. Mater.* **20**, 175–180 (2021).

36. Alam, P., Leung, N. C., Liu, J. K. et al. Two are better than one: a design principle for ultralong-persistent luminescence of pure organics. *Adv. Mater.* **32**, 2001026 (2020).

37. Chen, Y., Xie, Y., Shen, H., Lei, Y. et al. Tunable phosphorescence/fluorescence dual emissions of organic isoquinoline-benzophenone doped systems by akoxy engineering. *Chem. Eur. J.* **26**, 17376–17380 (2020).

38. Chen, B., Huang, W., Su, H. et al. An unexpected chromophore–solvent reaction leads to bicomponent aggregation-induced phosphorescence. *Angew. Chem. Int. Ed.* **59**, 10023–10026 (2020).

39. Wang, Y., Yang, Jie., Fang, Manman. et al. Forster resonance energy transfer: An efficient way to develop stimulus-responsive room-temperature phosphorescence materials and their applications. *Matter* **3**, 449−463 (2020).

40. Lei, Y., Dai, W., Tian, Y. et al. Revealing insight into long-lived room-temperature phosphorescence of host-guest systems. *J. Phys. Chem. Lett.* **10**, 6019−6025 (2019).

41. Lei, Y., Yang, J., Dai, W. et al. Efficient and organic host-guest room-temperature phosphorescence: tunable triplet-singlet crossing and theoretical calculations for molecular packing. *Chem. Sci.* DOI: 10.1039/d1sc01175h.

42. Wang, D., Xie, Y., Wu, X. et al. Excitation-dependent triplet-singlet intensity from organic host-guest materials: tunable color, white-light emission, and room-temperature phosphorescence. *J. Phys. Chem. Lett.* **12**, 1814−1821 (2021).

43. Lei, Y., Dai, W., Guan, J. et al. Wide-range color-tunable organic phosphorescence materials for printable and writable security inks. *Angew. Chem. Int. Ed.* **59**, 16054–16060 (2020).

44. Wei, J., Liang, B., Duan, R. et al. Induction of strong long-lived room-temperature phosphorescence of *N*-phenyl-2-naphthylamine molecules by confinement in a crystalline dibromobiphenyl matrix. *Angew. Chem. Int. Ed.* **128**, 15818−15822 (2016).

45. Xie, Z., Zhang, X. et al. Wide-range lifetime-tunable and responsive ultralong organic phosphorescent multi-host/guest system. *Nat. Commun.* **12**, 3522 (2021).

46. Wang, X., Sun, Y., Wang, G., Li, J., Li, X., Zhang, K. TADF-type organic afterglow. *Angew. Chem. Int. Ed.* DOI: 10.1002/anie.202105628.

47. Chen, B., Huang, W., Nie, X., Cheng, X., Liao, F., Miao, H., Zhang, X., Zhang, G. Organic guest-host system produces room-temperature phosphorescence at part-per-billion level. *Angew. Chem. Int. Ed.* DOI: 10.1002/anie.202106204.

48. Zhen, X., Tao, Y., An, Z., Chen, P., Xu, C., Chen, R., Huang, W., Pu, K. *Adv. Mater*, **29**, 1606665 (2017).

49. Dang, Q., Jiang, Y., Wang, J., Wang, J., Zhang, Q., Zhang, M., Luo, S., Xie, Y., Pu, K., Li, Q., Li, Z. Room-temperature phosphorescence resonance energy transfer for construction of near-infrared afterglow imaging agents. *Adv. Mater.* **32**, 2006752 (2020).

50. Liu, X., Dai, W., Qian, J., Lei, Y., Liu, M., Cai, Z., Huang, X., Wu, H., Dong, Y. Pure room temperature phosphorescence emission of an organic host–guest doped system with a quantum efficiency of 64%. *J. Mater. Chem. C* **9**, 3391−3395 (2021).

51. Wang, Y., Gao, H., Yang, J., Fang, M., Ding, D., Tang, B. Z., Li, Z. High performance of simple organic phosphorescence host–guest materials and their application in time-resolved bioimaging. *Adv. Mater.* **33**, 2007811 (2021).

Figures

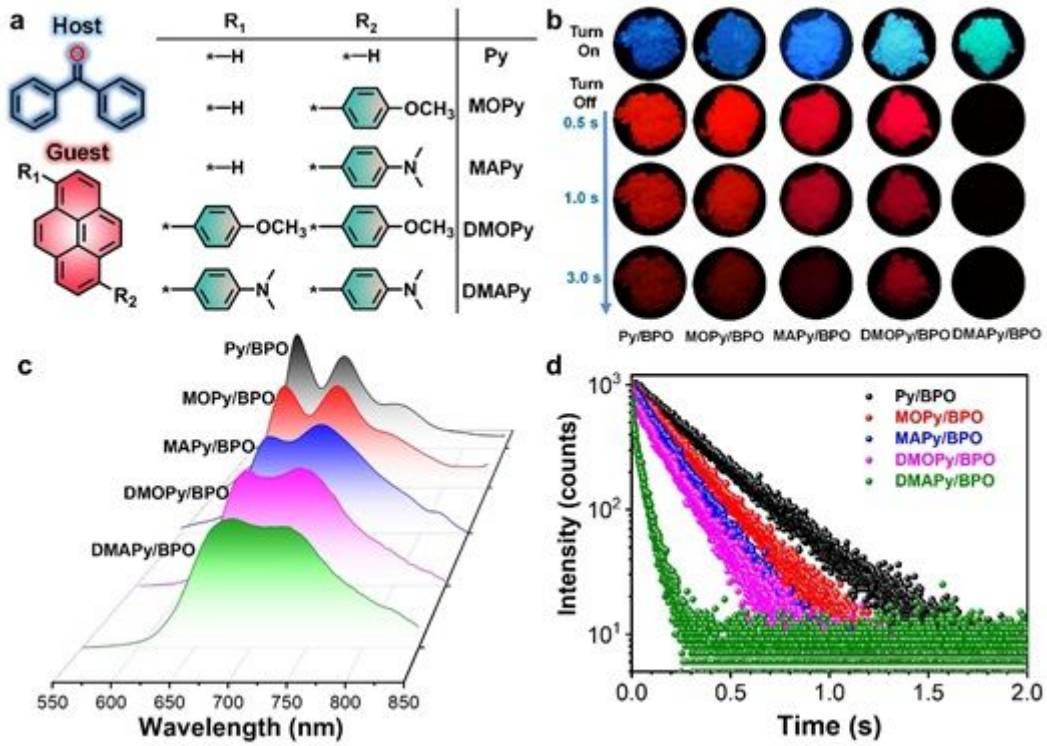

Figure 1

Photoluminescence properties of the guest-host system. a, Molecular structures of the guest and host molecules. b, Fluorescence (top) and phosphorescence (down) images of the guest–host materials. c, Phosphorescence spectra of host-guest materials. Excitation wavelength: 380 nm d, Phosphorescence decay curves of guest–host materials. Excitation wavelength: 380 nm.

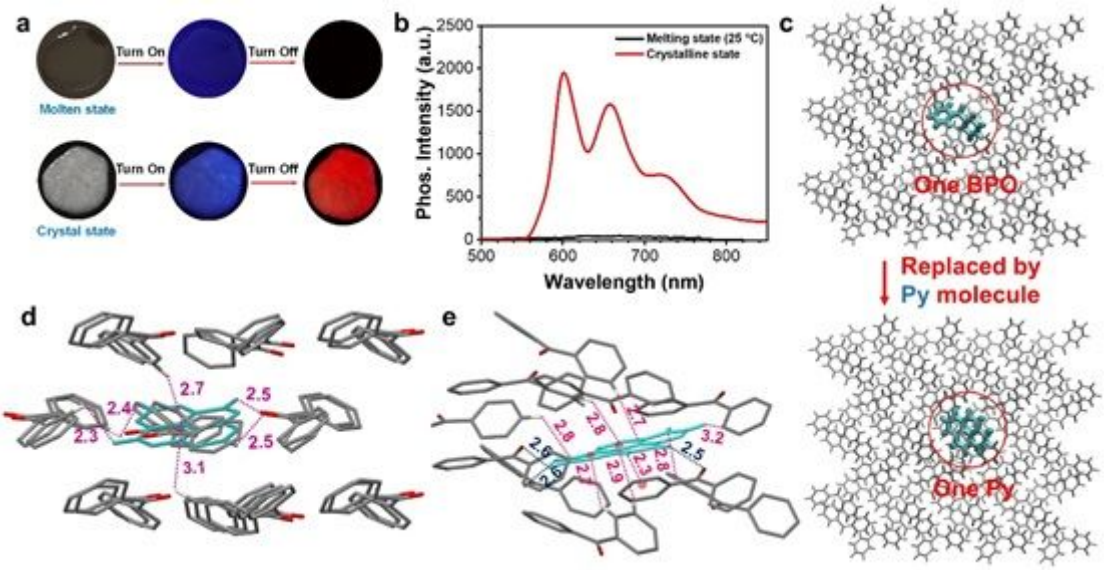

Figure 2

Non-radiative suppression of guest excitons by host matrix. a, Photographs of Py/BPO in different states. b, Phosphorescence spectra of Py/BPO. c, Model setup of Py/BPO guest–host system. d, Spatial distances between the Py molecule and the surrounding BPO molecules. e, Interaction distances of C-H–

π or C-H···O interactions between Py molecule and surrounding BPO molecules. The distances between each phenyl ring center of Py molecule and the hydrogen atom of the BPO molecules are marked by a red line. The corresponding distances between the oxygen atom of BPO and the hydrogen atoms of Py are marked by a blue line.

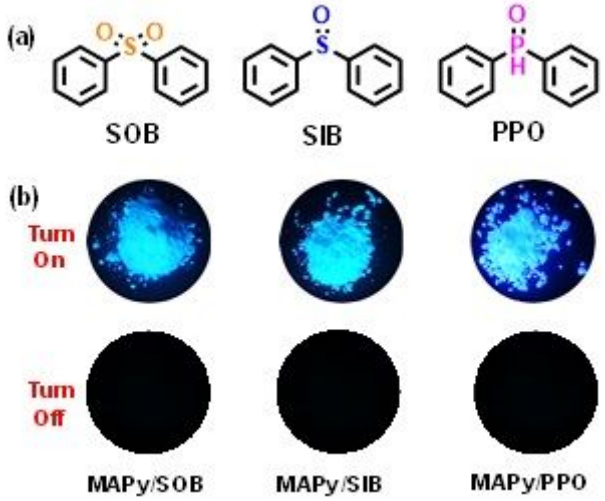

Figure 3

Luminescence properties of guest molecules in other hosts. a, Molecular structure of the reference hosts. b, Luminescent images of the reference guest–host materials.

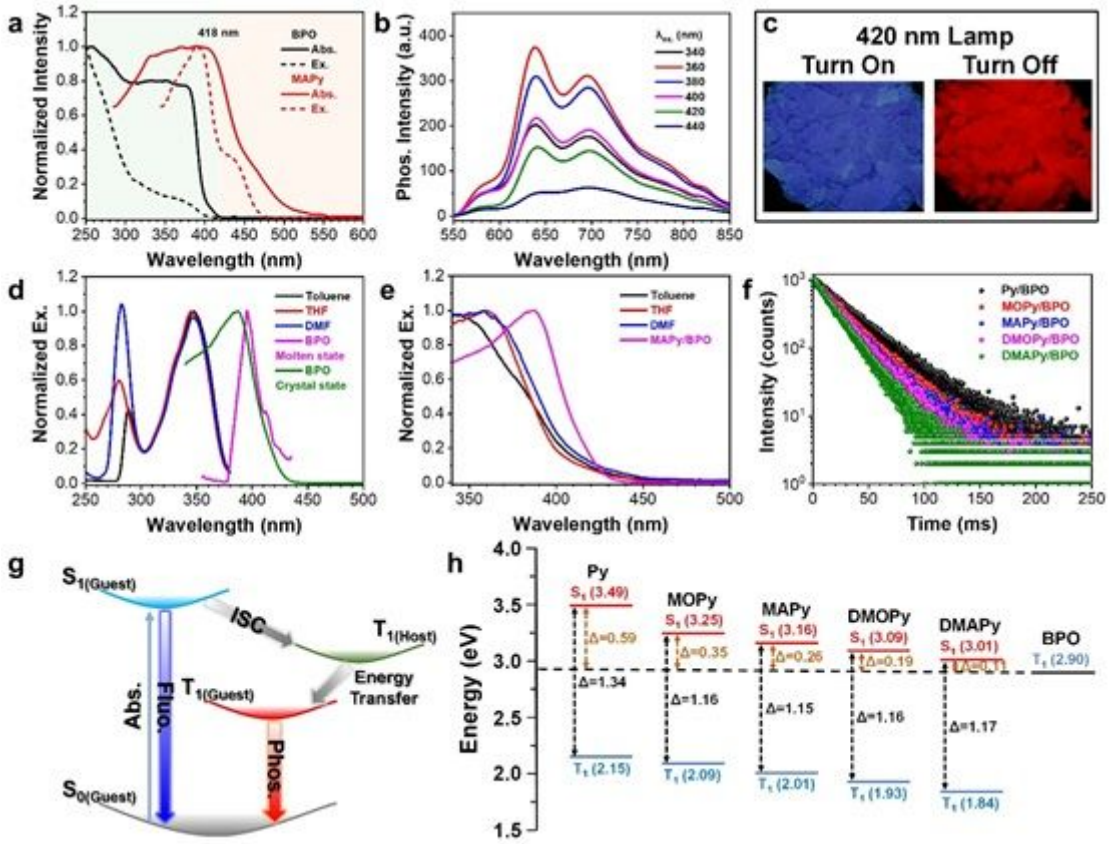

Figure 4

Energy transfer between guest and host. a, Excitation spectra of host BPO powder and guest MAPy powder. b, Phosphorescence spectra of guest-host material MAPy/BPO at different excitation wavelengths. c, Luminescence photos of the MAPy/BPO powder. Excitation spectra of fluorescence (d)/phosphorescence (e) of MAPy in different solvent and molten state host (Concentration: 1×10-4 mol/L). f, Phosphorescence decay curves of the guests in 77 K (Ex: 380 nm; Concentration: 1×10-4 mol/L; Solvent: 2-methyltetrahydrofuran). g, Proposed transfer path between guest and host. h, The energy levels of BPO and five guests.

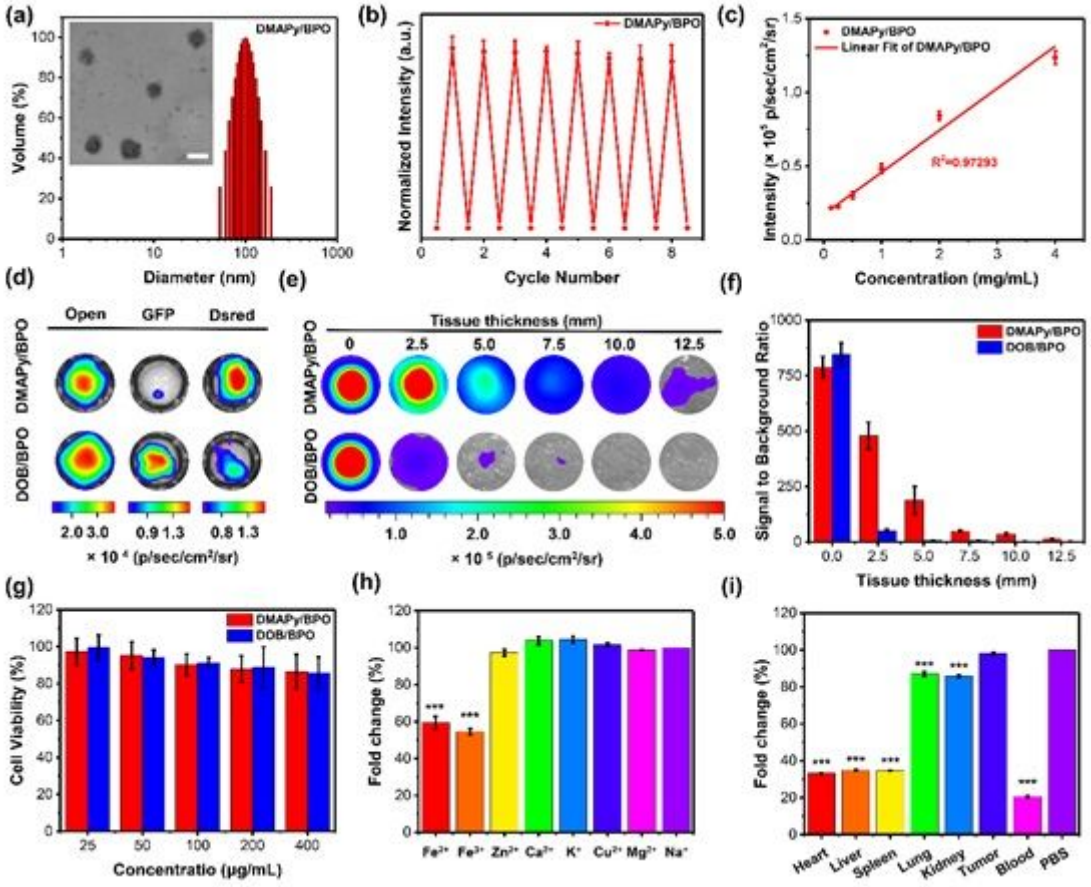

Figure 5

Phosphorescence properties of DMAPy/BPO and DOB/BPO nanoparticles. a, Diameter distribution of DMAPy/BPO nanoparticles. Inset: transmission electron microscopy image, scale bar = 100 nm. b, The normalized phosphorescence intensities of DMAPy/BPO NPs as a function of cycle number of UV light irradiation (n = 3). c, The phosphorescence intensities as a function of the concentration of DMAPy/BPO NPs (n = 3). d, Phosphorescence images of DMAPy/BPO and DOB/BPO NPs (4 mg mL−1) captured through different filters. e, Phosphorescence images of DMAPy/BPO and DOB/BPO NPs (10 mg mL−1) covered with different thicknesses of chicken tissue. f, SBR ratios from coverings with different tissue thicknesses given in (e). g. Cytotoxicities of DMAPy/BPO and DOB/BPO NPs against 4T1 cells. The 4T1 cells were incubated with DMAPy/BPO and DOB/BPO NPs at different concentrations for 8 h (n = 4). h. Fold change plot of phosphorescence intensities of DMAPy/BPO NPs in various metal ions. Error bars: mean ± standard deviation (n = 3). Triple asterisks represent p < 0.01 compared with Na+. i. Fold change

plot of phosphorescence intensities for DMAPy/BPO NPs in different tissue homogenates. Error bars: mean ± standard deviation (n = 3). Triple asterisks represent p < 0.01 compared with PBS.

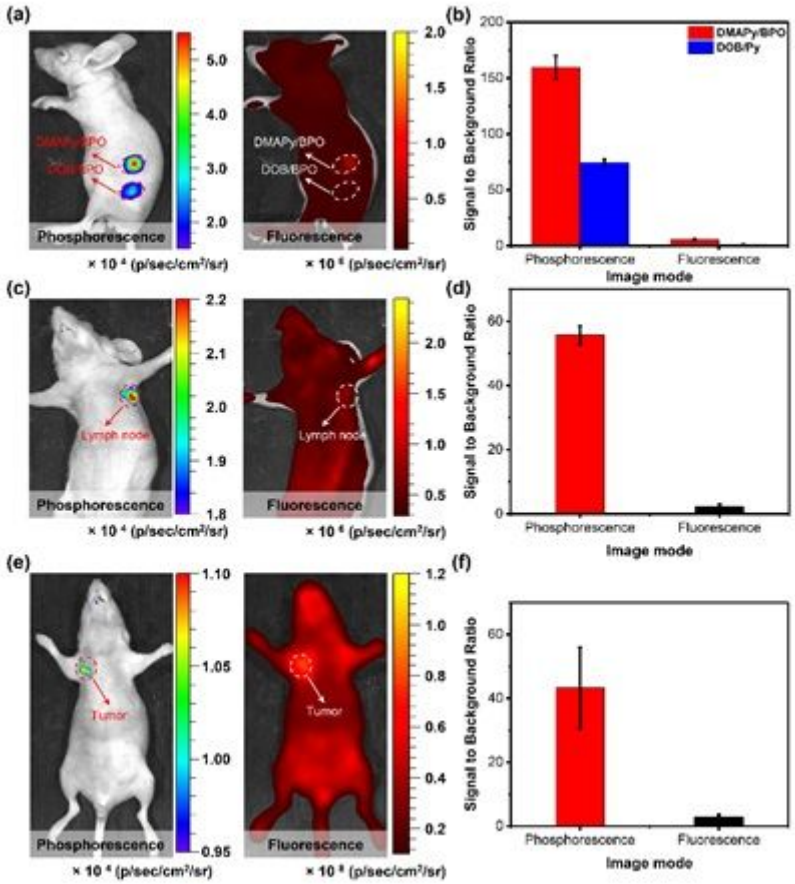

Figure 6

Applications in intravital phosphorescence imaging. a, Phosphorescence and fluorescence imaging of a mouse with the subcutaneous inclusions of DMAPy/BPO NPs and DOB/BPO NPs (4 mg mL−1). Circles indicate the locations of nanoparticle injection. b, Signal to background ratio for phosphorescence and fluorescence imaging of subcutaneous injection in live mice. c, Phosphorescence and fluorescence imaging of lymph nodes in mice 0.5 h after intradermal injection of DMAPy/BPO NPs (4 mg mL−1) into the forepaw of live mice. d, Signal to background ratio for phosphorescence and fluorescence imaging of lymph node in live mice. e, Phosphorescence and fluorescence imaging of live tumor-bearing mice 6 h after the injection of DMAPy/BPO NPs into the vein (4 mg mL−1). f, Signal to background ratio for phosphorescence and fluorescence imaging of tumor in live mice. All error bars were based on standard deviation (n = 3).

Supplementary Files

This is a list of supplementary files associated with this preprint. Click to download.

- MOPy.cif

- MAPy.cif
- DMOPy.cif
- DMAPy.cif
- checkreportMOPy.pdf
- checkreportMAPy.pdf
- checkreportDMOPy.pdf
- checkreportDMAPy.pdf
- Scheme1.pdf
- SINC.docx